UCSF
UC San Francisco Previously Published Works

Title
Tumor Microenvironment Biosensors for Hyperpolarized Carbon-13 Magnetic Resonance Spectroscopy

Permalink
https://escholarship.org/uc/item/5gz0m9nv

Journal
Molecular Imaging and Biology, 23(3)

ISSN
1536-1632

Authors
Mu, Changhua
Korenchan, David E
Wang, Sinan
et al.

Publication Date
2021-06-01

DOI
10.1007/s11307-020-01570-0

Peer reviewed

Tumor Microenvironment Biosensors for Hyperpolarized Carbon-13 Magnetic Resonance Spectroscopy

Changhua Mu[1], **David E. Korenchan**[1], **Sinan Wang**[1], **David M. Wilson**[1], **Robert R. Flavell**[1,2,*]

[1]Department of Radiology and Biomedical Imaging, University of California, San Francisco, California, USA

[2]Department of Pharmaceutical Chemistry, University of California, San Francisco, California, USA

Abstract

Hyperpolarization (HP) of a carbon-13 molecule via dynamic nuclear polarization (DNP) involves polarization at low temperature, followed by a dissolution procedure producing a solution with highly polarized spins at room temperature. This dissolution DNP method significantly increases the signal-to-noise ratio (SNR) of nuclear magnetic resonance (NMR) over 10,000-fold and facilitates the use of magnetic resonance spectroscopy (MRS) to image not only metabolism, but also the extracellular microenvironment. The extracellular tumor microenvironment (TME) closely interacts with tumor cells and stimulates their growth and metastasis. Thus, the ability to detect pathological changes in the TME is pivotal for the detection and study of cancers. This Review highlights the potential use of MRS to study features of the tumoral TME – elevated export of lactate, reduced interstitial pH, imbalanced redox equilibrium, and altered metal homeostasis. The promising outcomes of both *in vitro* and *in vivo* assays and suggest that DNP-MRS may be a useful technique to study aspects of the TME. With continued improvements, this tool has the potential to study the TME and provide guidance for accurate patient stratification and precise personal therapy.

Graphical Abstract

*To whom correspondence should be addressed: Robert R. Flavell, 185 Berry St., Suite 350, Box 0946, San Francisco, CA 94143, Robert.flavell@ucsf.edu.
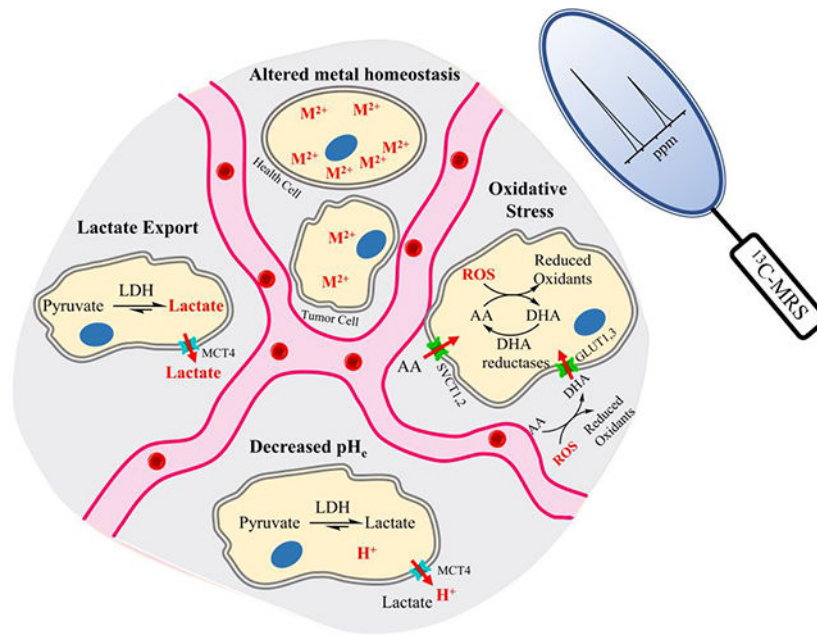
Keywords

hyperpolarization; dynamic nuclear polarization; magnetic resonance spectroscopy; biosensors; carbon-13 cellular substrates; tumor microenvironment

Introduction

The tumor microenvironment (TME) refers to the altered and pathological surroundings of growing tumor cells. It is mainly composed of tumor cells, tumor stroma, immune cells, and the extracellular matrix (ECM) [1]. The TME closely interacts with tumor cells and promotes tumor progression and therapeutic resistance [2]. In comparison to the normal tissue microenvironment, the TME exhibits many differences, including abnormal tissue architecture, elevated oxidative stress, extracellular acidification, metabolic alterations, and abnormal ECM dynamics [3]. A variety of strategies have been employed to study the tumor microenvironment using non-invasive imaging methods, including NMR spectroscopy of protons and other nuclei, chemical exchange saturation transfer (CEST), and nuclear imaging techniques such as positron emission tomography (PET) and single photon emission computed tomography (SPECT) [4, 5]. The initial successful translation of the dynamic nuclear polarization – magnetic resonance spectroscopy (DNP-MRS) technique to hyperpolarize (HP) [1-^{13}C]pyruvate for clinical imaging of patients with prostate cancer (PCa) in 2013 [6] led to a new era of the use of this method in patient studies, with promising outcomes summarized in prior review articles [7]. Expanding the scope of DNP-MRS to characterize the TME may provide complementary information that could enhance the ability to diagnose and treat cancer effectively. In this review, we focus on the development and implementation of ^{13}C-labeled TME biosensors.

Dynamic nuclear polarization of ^{13}C labeled cellular substrates is an emerging clinical technique, which can significantly increase ^{13}C NMR sensitivity over 10,000-fold, allowing for MRS detection *in vitro* and *in vivo* [8]. However, DNP-MRS has strict criteria for successful implementation, including the requirement for a high concentration preparation, the ability to form a glass upon freezing, low probe toxicity, long spin-lattice relaxation times (T_1) for the interrogated ^{13}C nucleus, and spectrally resolvable chemical shift differences upon reaction [9]. The study of the TME using DNP-MRS is a relatively new concept. Therefore, the purpose of this review is to (i) summarize the basics of the DNP-MRS imaging technique; (ii) elucidate the biochemical processes responsible for four important possible TME imaging biomarkers: elevated cellular export of lactate, reduced interstitial pH, imbalanced cellular redox equilibrium, and altered metal homeostasis; and (iii) highlight *in vitro* and *in vivo* assays using DNP-MRS to characterize the status of TME and their correlation with tumor behavior.

1. Nuclear Magnetic Resonance Spectroscopic Imaging using Hyperpolarized Carbon-13 Biosensors via Dynamic Nuclear Polarization

Non-proton MRS can be challenging for imaging owing to low sensitivity. Spin polarization can be employed to increase the signal-to-noise ratio (SNR). DNP and parahydrogen-induced polarization (PHIP) are commonly used methods for spin polarization. DNP is a powerful technique that can substantially increase the nuclear spin polarization of ^{13}C in cellular substrate molecules and improve its ^{13}C NMR signal sensitivity over 10,000 fold [8]. The DNP procedure involves cooling a mixture of ^{13}C biosensor compound, a free radical reagent, and in some cases a solvent or glass former to ~1 K. The sample is then irradiated with microwave frequency in a strong magnetic field to transfer the polarization from electron spins on the radicals to the ^{13}C nuclei of the biosensor molecules. Finally, it is warmed up rapidly (dissolution) for subsequent experimental steps (Figure 1a) [10, 11]. For example, we polarized [1-^{13}C]1,2-glycerol carbonate (GLC) to 29.5% at 5 T (back-calculated to time of dissolution), corresponding to ~29,400 fold enhancement of SNR after dissolution (Figure 1b). After dissolution, the polarization rapidly returns to its thermodynamic equilibrium, with exponential decay of hyperpolarized signal with time constant T_1 (Figure 1c). PHIP is an alternative modality to DNP, involving a catalyzed hydrogenation reaction by adding para-enriched hydrogen (para-H_2) to an unsaturated substrate molecule. However, the application of PHIP can be limited due to the availability of unsaturated precursors for the target substrate [12, 13]. An alternative approach called signal amplification by reversible exchange (SABRE) relies on transferring polarization from para-H_2 through the scalar coupling framework of a metal complex to the substrate, which can keep the substrate chemically unchanged [14]. In order to be eligible for animal models and human clinical imaging studies, the HP biosensor should preserve the polarization long enough for dissolution, intravenous injection, and imaging data collection. The basic criteria for using DNP-MRS are as follows: the HP ^{13}C biosensor molecules should (i) be nontoxic, with safety of injecting sufficiently high concentrations of 50–250 mM for detection; (ii) have rapid cell transport or enzyme-catalyzed conversion; (iii) have a sufficiently long spin-lattice relaxation (T_1); (iv) polarize well enough to generate sufficient signal enhancement (typically greater than 5% polarization); and (v) demonstrate an

observable chemical shift separation (5 ppm) between the agent and resulting HP metabolites [9]. In this Review, we focus on the application of dissolution DNP-MRS for interrogating the status of the TME.

2. Hyperpolarized ^{13}C MRS Biosensors for Imaging the Tumor Microenvironment

In this Review, we highlight four TME conditions, including elevated export of lactate, reduced interstitial pH, increased oxidative stress, and altered metal homeostasis. We describe the potential mechanism of using corresponding HP ^{13}C biosensors to target their biomarkers for the detection and of the tumor. The HP ^{13}C biosensor molecules and their fundamental mechanisms of action are summarized in Figure 2. DNP-MRS also boasts the capability of simultaneously studying the distorted tumor vasculature present within the TME using HP [^{13}C]urea or other probes, which have been used for measuring regional blood flow in preclinical cancer models [15].

2.1   Imaging HP ^{13}C-Lactate in the Tumor Microenvironment

Unconstrained tumor proliferation and invasion and therapeutic resistance usually correlate with alterations in cellular metabolism and extracellular conditions, indicative of the Warburg effect – an upregulation of aerobic glycolysis and lactic acid fermentation through the lactate dehydrogenase (LDH) catalyzed reaction [16]. Figure 3 shows the metabolic pathway of pyruvate and the function of the monocarboxylate transporters (MCT). Intravenously injected pyruvate rapidly metabolizes into lactate, alanine, and CO_2, with the metabolic rates and metabolite ratios depending on the function of the tissues. Owing to the increased uptake of pyruvate via MCT1 and MCT4 and increased activity of LDH in the tumor cells, the increased conversion of pyruvate to lactate (or a high ratio of [lactate]/[pyruvate]) is observed in tumors [17–19]. Thus, HP [1-^{13}C]pyruvate provides a method of estimating the flux through this pathway and characterizing the metabolic status of a tumor. This method has been successfully translated to human clinical application to noninvasively characterize alterations in tumor metabolism for patients [6].

An important link between heightened glycolytic flux and the TME is the increased cellular export of lactate, a process that can be investigated using DNP MRS. Increased concentrations of exported lactate in the TME conditions to support the tumor, for example, by suppressing immune effector cells [20] and influencing nearby stromal and vascular cells [21]. K. R. Keshari *et al* investigated the HP [1-^{13}C]pyruvate-to-HP [1-^{13}C]lactate flux in real-time using DNP-MRS combined with a bio-reactor platform of living renal cell carcinoma (RCC) cells. They found RCC cells have much a higher flux rate than the normal renal proximal tubule cells and the metastatic RCC cells have more rapid export of lactate to the extracellular space. These differences are likely mediated by the differential expression of MCT4 [22]. Subsequently, K. R. Keshari *et al* injected HP [1-^{13}C]pyruvate in a living human prostate tissue slice culture platform. They observed a significantly increased [1-^{13}C]pyruvate to [1-^{13}C]lactate flux in malignant in comparison to the benign prostate tissues and provided mechanistic evidence for HP[1-^{13}C]lactate as a prostate cancer biomarker [17]. R. Sriram *et al* developed a DNP-MRS compatible 3D cell/tissue culture

bio-reactor to dynamically interrogate HP [1-^{13}C]lactate production and efflux in human RCC cells, aiming at testing the correlation of this process with cancer aggressiveness, metastasis, and response to therapy [23]. Using this DNP-MRS bio-reactor platform, B. L. Koelsch *et al* were able to separate extra- and intracellular weighted HP metabolites of RCC cells and assess the ability of membrane transport in real-time [24]. These techniques have been extended to *in vivo* model systems to estimate lactate export in tumors and to provide a link to the TME. B. Feuerecker *et al* co-polarized [1-^{13}C]pyruvate and [1,4-^{13}C$_2$]fumarate, and measured the apparent diffusion coefficient (ADC) of the produced lactate using HP diffusion-weighted MRS. They linked the ADC ratio of lactate to pyruvate to the distribution of lactate in the intra- and extracellular compartments to report the transport, while measuring fumarate-to-malate conversion to detect necrosis and rule out its interference with lactate ADC [25]. More recently, R. Sriram *et al* used dynamic diffusion-weighted HP ^{13}C pyruvate MRI to interrogate tumor lactate production and compartmentalization in a murine orthotopic model of human RCCs [26]. Furthermore, X. Zhu *et al* used this method based on a slice-selective double spin echo sequence to monitor the cellular lactate transport on the transgenic adenocarcinoma of the prostate (TRAMP) model [27]. Taken together, these prior studies suggest feasibility for imaging lactate in the TME using hyperpolarized ^{13}C.

2.2 Imaging decreased interstitial pH (pH$_e$)

Solid tumors have heterogeneous perfusion, high metabolic activity, rapid cell proliferation, and typically develop an acidic interstitial microenvironment with pH 6.5 – 7.2, in contrast to pH 7.4 in normal and healthy tissues [28]. Extracellular acidification is commonly associated with local invasion and metastasis in a variety of cancers, including melanoma, breast, colon, renal, and PCa [29, 30]. Mechanisms of extracellular pH (pH$_e$) acidification include monocarboxylate transporters (MCTs) [31], Na$^+$/H$^+$ exchanger 1 [32], vacuolar H$^+$-ATPase [33], and outward-facing carbonic anhydrase isoforms [34]. Measurement of pH$_e$ exhibits value for detecting an invasive and potentially metastatic phenotype. Methods for imaging pH$_e$ include (i) pH sensitive contrast agents for ^{1}H MRI [35–37], and paramagnetic chemical exchange saturation transfer mechanism (paraCEST) [38]; (ii) other non-proton MRS, for example the ^{31}P biosensor, 3-aminopropyl phosphonate [39–43], and ^{19}F probes such as 3-[*N*-(4-fluoro-2-trifluoromethylphenyl)-sulphamoyl]-propionic acid (known as ZK-150471) [41, 44, 45] and 6-fluoropyridoxol [46, 47]; and (iii) hyperpolarized MRS, including the SABRE [48, 49] techniques introduced above, (iv) nuclear imaging techniques such as PET and SPECT [50, 51], and (v) dissolution DNP, which is the focus of this Review on ^{13}C-labeled biosensors.

A variety of methods have been employed for imaging of pH using DNP-MRS [10, 52–56]. The most widely reported biosensor for pH imaging using DNP-MRS is H^{13}CO$_3$$^-$. The core mechanism of the method is that mammalian tissues preserve a highly regulated acid-base balance via an equilibrated reaction between HCO$_3$$^-$ and CO$_2$, catalyzed by the enzyme carbonic anhydrase in the extracellular environment [57]. Theoretically, if exogenous HP H^{13}CO$_3$$^-$ can rapidly equilibrate in tissues and establish a chemical equilibrium with HP ^{13}CO$_2$, their detectable signals can be used to image pH$_e$ using the Henderson-Hasselbalch equation, pH = pK$_a$ + log$_{10}$([HCO$_3$$^-$]/[CO$_2$]), assuming pK$_a$ is known *in vivo* [58]. F. D. Gallagher *et al* intravenously injected HP H^{13}CO$_3$$^-$ in a mouse tumor model. First, they

measured the T_1s of H^{13}CO$_3^-$ and ^{13}CO$_2$ *in vivo* as 10.1 ± 2.9 s and 9.8 ± 2.5 s respectively at 9.4 T and found their apparent T_1s become equal due to the rapid interconversion, so that calculated pH would not vary in the course of HP decay. They then imaged pH$_e$ and demonstrated that the average tumor pH$_e$ was significantly lower than the surrounding tissue [10]. The same group quantified carbonic anhydrase activity through the rapid exchange rate of H^{13}CO$_3^-$ and ^{13}CO$_2$ catalyzed by carbonic anhydrase by analyzing the change in signal decay before and after selective saturation of the HP ^{13}CO$_2$ resonance. They have found that tumor cells overexpress carbonic anhydrase to compensate for decreased enzymatic activity due to the acidic extracellular TME [59].

Although HP H^{13}CO$_3^-$ has been demonstrated as a useful biosensor compound for *in vivo* pH$_e$ imaging using MRS [10, 60], H^{13}CO$_3^-$ has several challenges, including low polarization, difficulties in preparing for hyperpolarization at high concentration, fast T_1 relaxation, and the use of toxic reagents such as Cs for the formulation [60]. These challenges have been mitigated by developing methods that rapidly produce HP H^{13}CO$_3^-$ and HP ^{13}CO$_2$ indirectly from a more readily polarized precursor compound via a chemical reaction, while preserving the nuclear spin order (polarization). For example, R.K. Ghosh *et al.* exploited the rapid decarboxylation of HP [1,2-^{13}C] pyruvate with hydrogen peroxide (H$_2$O$_2$) to produce hyperpolarized [1-^{13}C] acetate, ^{13}CO$_2$, and H^{13}CO$_3^-$ [61]. More recently, tissue pH was measured *in vivo* using HP ^{13}C-ethyl acetyl carbonate. The compound was rapidly hydrolyzed by esterase *in vivo* to ^{13}C-monoacetyl carbonate, which then decomposed to HP ^{13}CO$_2$ [62]. Similarly, we polarized non-toxic ^{13}C-carbonated small organic precursor molecules, and subsequently hydrolyzed them to HP H^{13}CO$_3^-$ and biocompatible components via a base-catalyzed dissolution step [52, 54, 63]. We verified HP [1-^{13}C]1,2-glycerol carbonate (^{13}C-GLC) as an excellent candidate for this HP H^{13}CO$_3^-$ producing method since ^{13}C-GLC and its hydrolytic products including H^{13}CO$_3^-$, ^{13}CO$_2$, and glycerol are nontoxic at high concentration [64] and ^{13}C-GLC can rapidly (< 30 s) achieve >98 % breakdown at elevated temperature (~75 °C) in the presence of NaOH. In combination with hyperpolarized ^{13}C MRS, we employed this method to image pH$_e$ in the TRAMP model and correlated decreases in tumor pH to the increased grade of tumors (Figure 4). The subsequent *in vitro* assays and *in vivo* evaluation on PCa staging demonstrated this method can achieve a high polarization, produce high concentrations of HP H^{13}CO$_3^-$ in solution, and consequently obtain large signal gains for pH$_e$ imaging [52, 54]. One important general consideration in the use of precursor molecules to generate H^{13}CO$_3^-$ is the potential for the generation of side products during chemical production. In order to facilitate future clinical translation of these methods, careful optimization of reaction conditions would be necessary.

In addition to the method of measuring the ratio of HP H^{13}CO$_3^-$ to HP ^{13}CO$_2$ to calculate pH$_e$ using the Henderson-Hasselbalch equation, other HP compounds exhibiting a pH-dependent chemical shift can be used to measure pH. In principle, a pH dependent chemical shift method has advantages including a potentially greater SNR because the signal is not split between two resonances. In contrast, bicarbonate has the advantages of being a non-toxic, endogenous molecule, routinely used in clinical medicine, suggesting feasibility for clinical translation. These chemical shift pH probes include N-(2-acetamido-)2-aminoethanesulfonic acid (ACES) [53], zymonic acid (ZA) [56], and [2-^{13}C,

D$_{10}$]diethylmalonic acid [55], among others [65, 66], all of which exhibit a large pH-dependent ^{13}C chemical shift over the physiologic range. For example, co-polarization of [2-^{13}C, D$_{10}$]diethylmalonic acid with [1–^{13}C,D$_9$]*tert*-butanol, a reference compound with a pH-independent chemical shift, could accurately image pH via ^{13}C NMR and MRS in phantom experiments [55]. Importantly, S. Duwel *et al* imaged pH$_e$ within healthy rats' bladders and kidneys, and xenograft tumors using co-polarized ZA and urea. They demonstrated the feasibility of measuring pH$_e$ via monitoring the chemical shift variation of ZA signals relative to urea, or between ZA's two ^{13}C labeled sites upon pH changes. This method exhibits several advantages, in particular, the independence of concentration, temperature, ionic strength, and protein concentration [56]. Overall, these prior promising studies suggest a future potential for clinical translation of hyperpolarized ^{13}C pH imaging for the detection of the acidic tumoral microenvironment in aggressive tumors.

2.3 Imaging imbalanced redox processes

Oxidative stress arises when the production of cellular reactive oxygen species (ROS) such as hydroxyl (OH$^\bullet$), superoxide (O2$^{-\bullet}$), hydrogen peroxide (H$_2$O$_2$), and nitric monoxide (NO$^\bullet$), generated as metabolic by-products by biological systems overwhelm the intrinsic antioxidants. For example, mitochondria use oxygen to produce adenosine triphosphate, leading to the production of ROS [67]. Overproduction of free radicals can cause damage to biomolecules and lead to the development of chronic diseases including cancer [68, 69]. Moreover, some other non-radical molecules such as hydrogen peroxide (H$_2$O$_2$), nitric oxide, hypochlorous acid, and peroxynitrite that can generate free radicals under various conditions like the Fenton reaction may therefore cause oxidative stress [70]. The human body has built-in immune defense systems of counteracting oxidative stress by producing antioxidants as free radical scavengers to prevent and repair damages caused by radicals [71]. Consequently, rapid cancer cell proliferation and drug resistance are correlated with a highly reduced intracellular microenvironment as a result of a high-level accumulation of reducing agents such as glutathione [72, 73] and nicotinamide adenine dinucleotide phosphate (NADPH) [74] to maintain the reduction-oxidation (redox) balance [75]. This intracellular reducing environment is generally coupled with an oxidizing TME.

Ascorbic acid (AA) is an essential reducing agent (antioxidant) and cofactor of numerous enzymes to activate biosynthetic reactions [76–79]. Importantly, as shown in Figure 5a, AA and its oxidized form, dehydroascorbic acid (DHA), are closely coupled to two primary cellular antioxidants: glutathione (GSH) and NADPH [76]. Cells have two types of transporters to uptake AA: sodium-dependent vitamin C transporters (SVCT1, 2) directly transport AA into cells [80], while most tissues acquire AA through the transport of DHA into cells via glucose transporters (GLUT1, GLUT2, and GLUT4), which exhibit a similar affinity for both DHA and glucose and are overexpressed in most tumors [81, 82]. Inside the cells, DHA is rapidly reduced to AA through two reactions with either GSH or GSH-dependent enzymes including the thiol-disulfide oxidoreductases, glutaredoxin, and protein disulfide isomerase, and the predominant NADPH-dependent enzyme such as selenoprotein and thioredoxin reductase [76, 83, 84]. Thus, the rate of intracellular reduction of DHA to AA reflects oxidative stress since it is determined by the availability of NADPH [85, 86].

Importantly, the properties of AA and DHA make them the prime candidates for *in vivo* metabolic investigation using DNP-MRS [84, 87]. DHA shares the same membrane transporters with glucose and therefore exhibits rapid uptake [88], and the interconversion between DHA and AA is also rapid, enabling detection of intracellular DHA reduction on the hyperpolarized timescale. Therefore, researchers have evaluated the feasibility of using [1-^{13}C]-DHA and [1-^{13}C]-AA as ideal redox couple biosensor candidates for hyperpolarized redox imaging and considered their potential for clinical translation. For example, two significant initial research works published in 2011 elucidated the above-described redox mechanism, demonstrated a relatively high level of hyperpolarization of [1-^{13}C]-DHA and [1-^{13}C]-AA, and importantly proved the hypothesized mechanism. K. R. Keshari *et al* [87] interrogated the *in vivo* rapid transformation of HP [1-^{13}C] DHA to HP [1-^{13}C] AA in different organs and tumors, such as in liver, kidney, within tumor and in TRAMP model, as well as in normal rat brains, where DHA are well perfused (Figure 5b). TRAMP mice exhibited an increased conversion ratio of AA/[AA + DHA] within the tumor in comparison to the normal prostate gland or the surrounding benign tissue, but there was no significant difference in the liver and kidney between TRAMP and normal mice. Thus, the feature suggests the feasibility of using HP [1-^{13}C] DHA as a biosensor for the detection of PCa. The cardiopulmonary effects of DHA on mice under anesthesia are well-known, but use of this redox sensor in humans may be possible in the future based on better preparative methods, and more sensitive hyperpolarized ^{13}C imaging tools. Interestingly, a high and rapid reduction of HP [1-^{13}C] DHA within the brain was observed, identifying DHA as an excellent biosensor to cross the blood-brain barrier to detect the oxidative stress inside the brain [89].

Another research work reported by S. E. Bohndiek *et al* [84] implicated AA and DHA could be used as extra- and intercellular biosensor candidates respectively. They observed that the extracellular pool of [1-^{13}C]-AA was oxidized rapidly in suspensions of hypoxic EL4 lymphoma cells, suggesting the generation of oxidative stress with hydrogen peroxide from cancer cells that deplete oxygen and nutrients from medium [90, 91]. They also found that intracellular [1-^{13}C]-DHA was reduced rapidly in both EL4 tumor cell suspension and *in vivo* EL4 tumor xenografts. Therefore, these results suggest HP [1-^{13}C]-AA could be used for detecting ROS in the extracellular environment, where high concentrations of superoxide and hydrogen peroxide may be present [90]. Additionally, imaging AA/DHA metabolism provides an approach for determining *in vivo* metabolism of NADPH and the ratio of GSSG/GSH ratio, both of which indicate oxidative stress [92]. In a follow up study from our groups, we extended the hyperpolarized ^{13}C AA approach to a similar ^{11}C PET imaging approach, where we found that extracellular [1-^{11}C]AA could be oxidized to [1-^{11}C]AA, and then internalized [93]. Thus, HP [1-^{13}C]-DHA and AA (and potentially, their ^{11}C analogs) might be used to image redox status *in vivo* for the characterization of cancers including PCa [87, 94].

Hydrogen peroxide (H$_2$O$_2$) is an important metabolite involved in cellular redox metabolism reactions and processes. The concentrations of H$_2$O$_2$ in the intra- and extracellular spaces play a crucial role in determining the proliferation, survival, or death of the cells [95]. The intracellular homeostatic concentration ranges from 0.1 ~ 100 nM, depending on the cell type, while about 100-fold concentration gradient from extracellular to intracellular has been

estimated. A higher concentration of H_2O_2 evokes inflammatory responses and leads to tumor growth, metastasis, growth arrest, and cell death [96]. Thus, the concentration of H_2O_2 acts as a potential biomarker for detecting the presence and progress of a variety of pathological changes. Accordingly, ^{13}C biosensors have been developed for imaging H_2O_2. A. R. Lippert *et al* imaged oxidative H_2O_2 using HP ^{13}C-benzoylformic acid as a ^{13}C MRI contrast agent, which selectively and rapidly reacts with H_2O_2 to produce HP ^{13}C-benzoic acid [97]. Wibowo *et al* developed ^{13}C thiourea (TU) to image the dynamics of H_2O_2 *in vivo* with high sensitivity and spatiotemporal resolution. They demonstrated that ^{13}C-TU is highly polarizable ($10.4 \pm 1.1\%$ polarization) with a long T_1 (53.8 ± 3.7 s at 3T). HP ^{13}C TU is oxidized by H_2O_2 to produce chemically distinguishable product HP ^{13}C thiourea dioxide that is subsequently hydrolyzed to urea [98]. Overall, the biological relevance of these H_2O_2 measurements, and limits of *in vivo* detection remain an area for future study. Taken together, these prior studies demonstrate a potential to use hyperpolarized ^{13}C MRI for the detection of alterations in redox homeostasis in the TME.

2.4 Imaging Alterations of Trace Divalent Metal Ions

Trace divalent ions, such as zinc, calcium, copper, iron, and selenium, play a vital role in many biochemical reactions for maintaining biological processes and function. Alterations in metal homeostasis are associated with pathological changes in the metabolic microenvironment of cancers [99–101]. Thus, the distribution of these metal ions could be potential biomarkers used for the detection of cancers and the prediction of therapy [102].

In principle, DNP-MRS could be well suited to the detection of metals. Two prior publications reported by A. Mishra *et al* [103] and S. Wang *et al* [104] established a solid foundation for the further development of this area. Mishra *et al* initially demonstrated the feasibility of using HP ^{13}C-labeled metal chelators EDTA and EGTA to identify divalent metals including, Pb^{2+}, As^{2+}, Cd^{2+}, Zn^{2+}, Mg^{2+}, and Ca^{2+} via the distinct carboxyl resonance variation by metal coordination (Figure 6a). They subsequently applied this technique to differentiate between biologically essential and toxic divalent metals and determined the concentration of Ca^{2+} in human serum [103]. However, one challenge potentially limiting the application of this method as an *in vivo* biosensor is the high concentration of Ca^{2+}, leading to challenges in generating image contrast.

S. Wang *et al* focused on the development of hyperpolarized amino acid-derived sensors for the detection of Zn^{2+} [104]. In normal prostate, zinc accumulates intracellularly to a remarkably high concentration, and then coordinates with citrate to be secreted into the prostatic fluid. In contrast, the zinc accumulation property becomes dysfunctional in de-differentiated PCa, leading to a 60–80% decrease in zinc concentration [105]. S. Wang *et al* identified [1-13C]L-cysteine ([1-13C]Cys) and [1-13C_2] iminodiacetic acid ([1-13C]IDA) as compounds with specificity and targetability of Zn^{2+} binding over other endogenous cations Na^+, K^+, Ca^{2+}, and Mg^{2+} and negligible chemical shift changes over the physiological pH range from 6.5 to 7.4. Importantly, these two biosensors showed (i) a good level of hyperpolarization ($13.4 \pm 0.6\%$ and $6.6 \pm 0.9\%$ back-calculated polarization for Cys and IDA, respectively), (ii) a large chemical change in the presence of Zn^{2+} (+4.6 and +7.3 ppm in the presence of equimolar Zn^{2+}, respectively), (iii) the linear correlation of the chemical

shift differences ([1-^{13}C]Cys) or area% of bound peak ([1-^{13}C]IDA) as the function of the concentrations of Zn^{2+} at low concentration range (0.25 and 0.5 eq.), and (iv) sufficient T_1 for MRI scans. However, due to substantial signal line broadening, [1-^{13}C]IDA exhibited limited applicability. In subsequent assays, it was verified that HP [1-^{13}C]Cys could accurately determine Zn^{2+} concentration in biological samples – rat serum and prostate extracts with low and high concentrations. The current results suggest feasibility of using HP ^{13}C metal chelators as potential biosensors to image pathologies associated with alterations in metal ions homeostasis such as PCa, neurodegenerative diseases, and diabetes.

3. Summary and Prospect of HP TME biosensors in Medical Applications

The TME plays a critical role in the processes of cancerous growth, invasion, and metastasis. The DNP-MRS methods described in this review could be used to interrogate the abnormal TME. In turn, they could provide information for disease prognostication and precise personal therapy. The TME imaging methods described in this review have the potential for clinical utility. For example, decreases in tumor pH_e measured with HP pH imaging methods could be used to detect transformation from indolent to aggressive cancer phenotypes in diseases such as prostate or breast cancer. This is under active investigation in our laboratories. In order to drive these methods into broader use in a clinical setting, an impact on patient management would be needed, for example, to detect locally aggressive disease, to help guide appropriate surgical or oncologic management. In this review, we considered four cancer properties in TME, including elevated export of lactate, reduced interstitial pH, increased oxidization stress, and altered metal homeostasis. Imaging of these pathologies with HP MRS has strong potential to be included in future clinical studies.

Acknowledgement

6. References

1. Arneth B, Tumor Microenvironment. Medicina, 2019. 56.

2. Whiteside TL, The tumor microenvironment and its role in promoting tumor growth. Oncogene, 2008. 27: 5904. [PubMed: 18836471]

3. Chen F, et al., New horizons in tumor microenvironment biology: challenges and opportunities. BMC Med, 2015. 13: 1. [PubMed: 25563062]

4. Zhou Z, et al., Molecular imaging of the tumor microenvironment. Adv Drug Deliv Rev, 2017. 113: 24. [PubMed: 27497513]

5. Penet M-F, et al., Molecular imaging of the tumor microenvironment for precision medicine and theranostics. Adv. Cancer Res, 2014. 124: 235. [PubMed: 25287691]

6. Nelson SJ, et al., Metabolic imaging of patients with prostate cancer using hyperpolarized [1–13C]pyruvate. Sci. Transl. Med, 2013. 5: 198ra108.

7. Brindle KM, et al., Tumor imaging using hyperpolarized 13C magnetic resonance spectroscopy. Magn Reson Med, 2011. 66: 505. [PubMed: 21661043]

8. Ardenkjaer-Larsen JH, et al., Increase in signal-to-noise ratio of > 10,000 times in liquid-state NMR. Proc. Natl. Acad. Sci. U. S. A, 2003. 100: 10158. [PubMed: 12930897]

9. Keshari KR, et al., Chemistry and biochemistry of 13C hyperpolarized magnetic resonance using dynamic nuclear polarization. Chem. Soc. Rev, 2014. 43: 1627. [PubMed: 24363044]

10. Gallagher FA, et al., Magnetic resonance imaging of pH in vivo using hyperpolarized 13C-labelled bicarbonate. Nature, 2008. 453: 940. [PubMed: 18509335]

11. Overhauser AW, Polarization of nuclei in metals. Phys. Rev, 1953. 92: 411.

12. Reineri F, et al., ParaHydrogen Induced Polarization of 13C carboxylate resonance in acetate and pyruvate. Nat. Commun, 2015. 6: 5858. [PubMed: 25556844]

13. Eills J, et al., Real-Time Nuclear Magnetic Resonance Detection of Fumarase Activity Using Parahydrogen-Hyperpolarized [1–13C]Fumarate. J. Am. Chem. Soc, 2019. 141: 20209. [PubMed: 31762271]

14. Adams RW, et al., Reversible Interactions with para-Hydrogen Enhance NMR Sensitivity by Polarization Transfer. Science, 2009. 323: 1708. [PubMed: 19325111]

15. von MC, et al., Imaging of blood flow using hyperpolarized [(13)C]urea in preclinical cancer models. J Magn Reson Imaging, 2011. 33: 692. [PubMed: 21563254]

16. Gatenby RA, et al., Why do cancers have high aerobic glycolysis? Nat. Rev. Cancer, 2004. 4: 891. [PubMed: 15516961]

17. Keshari KR, et al., Metabolic Reprogramming and Validation of Hyperpolarized 13C Lactate as a Prostate Cancer Biomarker Using a Human Prostate Tissue Slice Culture Bioreactor. Prostate, 2013. 73: 1171. [PubMed: 23532911]

18. Bok R, et al., The role of lactate metabolism in prostate cancer progression and metastases revealed by dual-agent hyperpolarized 13C MRSI. Cancers, 2019. 11: 257.

19. Hong CS, et al., MCT1 Modulates Cancer Cell Pyruvate Export and Growth of Tumors that Co-express MCT1 and MCT4. Cell Rep, 2016. 14: 1590. [PubMed: 26876179]

20. Fischer K, et al., Inhibitory effect of tumor cell-derived lactic acid on human T cells. Blood, 2007. 109: 3812. [PubMed: 17255361]

21. Koukourakis MI, et al., Comparison of Metabolic Pathways between Cancer Cells and Stromal Cells in Colorectal Carcinomas: a Metabolic Survival Role for Tumor-Associated Stroma. Cancer Res, 2006. 66: 632. [PubMed: 16423989]

22. Keshari KR, et al., Hyperpolarized 13C-Pyruvate Magnetic Resonance Reveals Rapid Lactate Export in Metastatic Renal Cell Carcinomas. Cancer Res, 2013. 73: 529. [PubMed: 23204238]

23. Sriram R, et al., Real-time measurement of hyperpolarized lactate production and efflux as a biomarker of tumor aggressiveness in an MR compatible 3D cell culture bioreactor. NMR Biomed, 2015. 28: 1141. [PubMed: 26202449]

24. Koelsch BL, et al., Separation of extra- and intracellular metabolites using hyperpolarized 13C diffusion weighted MR. J. Magn. Reson, 2016. 270: 115. [PubMed: 27434780]

25. Feuerecker B, et al., Hyperpolarized 13C diffusion MRS of co-polarized pyruvate and fumarate to measure lactate export and necrosis. J. Cancer, 2017. 8: 1. [PubMed: 28123592]

26. Sriram R, et al., Non-Invasive Assessment of Lactate Production and Compartmentalization in Renal Cell Carcinomas Using Hyperpolarized (13)C Pyruvate MRI. Cancers, 2018. 10.

27. Zhu X, et al., Dynamic diffusion-weighted hyperpolarized (13) C imaging based on a slice-selective double spin echo sequence for measurements of cellular transport. Magn Reson Med, 2019. 81: 2001. [PubMed: 30368893]

28. Gatenby RA, et al., Acid-Mediated Tumor Invasion: a Multidisciplinary Study. Cancer Res, 2006. 66: 5216. [PubMed: 16707446]

29. Kato Y, et al., Acidic extracellular microenvironment and cancer. Cancer Cell Int, 2013. 13: 89. [PubMed: 24004445]

30. Webb BA, et al., Dysregulated pH: a perfect storm for cancer progression. Nat. Rev. Cancer, 2011. 11: 671. [PubMed: 21833026]

31. Halestrap AP, et al., The monocarboxylate transporter family-Role and regulation. IUBMB Life, 2012. 64: 109. [PubMed: 22162139]

32. Cardone RA, et al., The role of disturbed pH dynamics and the Na+/H+ exchanger in metastasis. Nat. Rev. Cancer, 2005. 5: 786. [PubMed: 16175178]

33. Forgac M, Vacuolar ATPases: rotary proton pumps in physiology and pathophysiology. Nat. Rev. Mol. Cell Biol, 2007. 8: 917. [PubMed: 17912264]

34. Supuran CT, Carbonic anhydrases: novel therapeutic applications for inhibitors and activators. Nat. Rev. Drug Discovery, 2008. 7: 168. [PubMed: 18167490]

35. Garcia-Martin ML, et al., High resolution pHe imaging of rat glioma using pH-dependent relaxivity. Magn. Reson. Med, 2006. 55: 309. [PubMed: 16402385]

36. Raghunand N, et al., Renal and systemic pH imaging by contrast-enhanced MRI. Magn. Reson. Med, 2003. 49: 249. [PubMed: 12541244]

37. Martinez GV, et al., Imaging the extracellular pH of tumors by MRI after injection of a single cocktail of T1 and T2 contrast agents. NMR Biomed, 2011. 24: 1380. [PubMed: 21604311]

38. Aime S, et al., Paramagnetic Lanthanide(III) complexes as pH-sensitive chemical exchange saturation transfer (CEST) contrast agents for MRI applications. Magn. Reson. Med, 2002. 47: 639. [PubMed: 11948724]

39. Bhujwalla ZM, et al., Estimations of intra- and extracellular volume and pH by 31P magnetic resonance spectroscopy: effect of therapy on RIF-1 tumors. Br. J. Cancer, 1998. 78: 606. [PubMed: 9744499]

40. Lutz NW, et al., Quantitative In Vivo Characterization of Intracellular and Extracellular pH Profiles in Heterogeneous Tumors: A Novel Method Enabling Multiparametric pH Analysis. Cancer Res, 2013. 73: 4616. [PubMed: 23752692]

41. Ojugo ASE, et al., Measurement of the extracellular pH of solid tumours in mice by magnetic resonance spectroscopy: a comparison of exogenous 19F and 31P probes. NMR Biomed, 1999. 12: 495. [PubMed: 10668042]

42. McCoy CL, et al., The effect of blood flow modification on intra- and extracellular pH measured by 31P magnetic resonance spectroscopy in murine tumours. Br J Cancer, 1995. 72: 905. [PubMed: 7547238]

43. Gillies RJ, et al., 31P-MRS measurements of extracellular pH of tumors using 3-aminopropylphosphonate. Am. J. Physiol, 1994. 267: C195. [PubMed: 8048479]

44. Frenzel T, et al., Noninvasive in vivo pH measurements using a fluorinated pH probe and fluorine-19 magnetic resonance spectroscopy. Invest. Radiol, 1994. 29: S220. [PubMed: 7928237]

45. Aoki Y, et al., Measurement of intratumor pH by pH indicator used 19F-magnetic resonance spectroscopy: Measurement of extracellular pH decrease caused by hyperthermia combined with hydralazine. Invest. Radiol, 1996. 31: 680. [PubMed: 8915749]

46. Mehta VD, et al., 6-Fluoropyridoxol: a novel probe of cellular pH using 19F NMR spectroscopy. FEBS Lett, 1994. 349: 234. [PubMed: 8050572]

47. Hunjan S, et al., Simultaneous intracellular and extracellular pH measurement in the heart by 19F NMR of 6-fluoropyridoxol. Magn. Reson. Med, 1998. 39: 551. [PubMed: 9543416]

48. Shchepin RV, et al., 15N Hyperpolarization of Imidazole-15N2 for Magnetic Resonance pH Sensing via SABRE-SHEATH. ACS Sens, 2016. 1: 640. [PubMed: 27379344]

49. Olaru AM, et al., SABRE hyperpolarisation of vitamin B3 as a function of pH. Chem. Sci, 2017. 8: 2257. [PubMed: 28507682]

50. Vavere AL, et al., A Novel Technology for the Imaging of Acidic Prostate Tumors by Positron Emission Tomography. Cancer Res, 2009. 69: 4510. [PubMed: 19417132]

51. Flavell RR, et al., Caged [18F]FDG Glycosylamines for Imaging Acidic Tumor Microenvironments Using Positron Emission Tomography. Bioconjugate Chem, 2016. 27: 170.

52. Korenchan DE, et al., Dynamic nuclear polarization of biocompatible 13C-enriched carbonates for in vivo pH imaging. Chem. Commun, 2016. 52: 3030.

53. Flavell RR, et al., Application of Good's buffers to pH imaging using hyperpolarized 13C MRI. Chem. Commun, 2015. 51: 14119.

54. Korenchan DE, et al., Hyperpolarized in vivo pH imaging reveals grade-dependent acidification in prostate cancer. Oncotarget, 2019. 10: 6096. [PubMed: 31692908]

55. Korenchan DE, et al., Dicarboxylic acids as pH sensors for hyperpolarized 13C magnetic resonance spectroscopic imaging. Analyst, 2017. 142: 1429. [PubMed: 28322385]

56. Duwel S, et al., Imaging of pH in vivo using hyperpolarized (13)C-labelled zymonic acid. Nat Commun, 2017. 8: 15126. [PubMed: 28492229]

57. Swietach P, et al., New insights into the physiological role of carbonic anhydrase IX in tumour pH regulation. Oncogene, 2010. 29: 6509. [PubMed: 20890298]

58. Stabenau EK, T.A.H., Determination of the constants of the henderson-hasselbalch equation, (alpha)co2 and pka, in sea turtle plasma. J. exp. Biol, 1993. 180.

59. Gallagher FA, et al., Carbonic Anhydrase Activity Monitored In Vivo by Hyperpolarized 13C-Magnetic Resonance Spectroscopy Demonstrates Its Importance for pH Regulation in Tumors. Cancer Res, 2015. 75: 4109. [PubMed: 26249175]

60. Gallagher FA, et al., Imaging pH with hyperpolarized 13C. NMR Biomed, 2011. 24: 1006. [PubMed: 21812047]

61. Ghosh RK, et al., Efficient production of hyperpolarized bicarbonate by chemical reaction on a DNP precursor to measure pH. Magn. Reson. Med, 2015. 74: 1406. [PubMed: 25393101]

62. Maptue N, et al., Esterase-Catalyzed Production of Hyperpolarized 13C-Enriched Carbon Dioxide in Tissues for Measuring pH. ACS Sens, 2018. 3: 2232. [PubMed: 30398335]

63. Korenchan DE, et al., Using bidirectional chemical exchange for improved hyperpolarized [(13) C]bicarbonate pH imaging. Magn Reson Med, 2019. 82: 959. [PubMed: 31050049]

64. Sloviter HA, et al., Effects of the intravenous administration of glycerol solutions to animals and man. J. Clin. Invest, 1958. 37: 619. [PubMed: 13539201]

65. Hundshammer C, et al., Hyperpolarized amino acid derivatives as multivalent magnetic resonance ph sensor molecules. Sensors, 2018. 18: 600/1.

66. Chen J, et al., Simultaneous Assessment of Intracellular and Extracellular pH Using Hyperpolarized [1–13C]Alanine Ethyl Ester. Anal. Chem, 2020. 92: 11681. [PubMed: 32786486]

67. Pham-Huy LA, et al., Free radicals, antioxidants in disease and health. Int. J. Biomed. Sci, 2008. 4: 89. [PubMed: 23675073]

68. Fridovich I, Fundamental aspects of reactive oxygen species, or what's the matter with oxygen? Ann. N. Y. Acad. Sci, 1999. 893: 13. [PubMed: 10672226]

69. Fang Y-Z, et al., Free radicals, antioxidants, and nutrition. Nutrition, 2002. 18: 872. [PubMed: 12361782]

70. Lloyd RV, et al., The origin of the hydroxyl radical oxygen in the Fenton reaction. Free Radical Biol. Med, 1997. 22: 885. [PubMed: 9119257]

71. Valko M, et al., Free radicals, metals and antioxidants in oxidative stress-induced cancer. Chem.-Biol. Interact, 2006. 160: 1. [PubMed: 16430879]

72. Balendiran GK, et al., The role of glutathione in cancer. Cell Biochem. Funct, 2004. 22: 343. [PubMed: 15386533]

73. Ballatori N, et al., Glutathione dysregulation and the etiology and progression of human diseases. Biol. Chem, 2009. 390: 191. [PubMed: 19166318]

74. Sattler UGA, et al., The anti-oxidant capacity of tumour glycolysis. Int. J. Radiat. Biol, 2009. 85: 963. [PubMed: 19895273]

75. Cairns RA, et al., Regulation of cancer cell metabolism. Nat. Rev. Cancer, 2011. 11: 85. [PubMed: 21258394]

76. Linster CL, et al., Vitamin C. Biosynthesis, recycling and degradation in mammals. FEBS J, 2007. 274: 1.

77. Murad S, et al., Regulation of collagen synthesis by ascorbic acid. Proc. Natl. Acad. Sci. U. S. A, 1981. 78: 2879. [PubMed: 6265920]

78. Tolbert LC, et al., Effect of ascorbic acid on neurochemical, behavioral, and physiological systems mediated by catecholamines. Life Sci, 1979. 25: 2189. [PubMed: 542096]

79. Kojo S, Vitamin C: basic metabolism and its function as an index of oxidative stress. Curr. Med. Chem, 2004. 11: 1041. [PubMed: 15078165]

80. Tsukaguchi H, et al., A family of mammalian Na+-dependent L-ascorbic acid transporters. Nature 1999. 399: 70. [PubMed: 10331392]

81. Rumsey SC, et al., Absorption, transport, and disposition of ascorbic acid in humans. J. Nutr. Biochem, 1998. 9: 116.

82. Liang W-J, et al., Vitamin C transport systems of mammalian cells. Mol. Membr. Biol, 2001. 18: 87. [PubMed: 11396616]

83. Corti A, et al., Cellular pathways for transport and efflux of ascorbate and dehydroascorbate. Arch. Biochem. Biophys, 2010. 500: 107. [PubMed: 20494648]

84. Bohndiek SE, et al., Hyperpolarized [1–13C]-Ascorbic and Dehydroascorbic Acid: Vitamin C as a Probe for Imaging Redox Status in Vivo. J. Am. Chem. Soc, 2011. 133: 11795. [PubMed: 21692446]

85. Tong X, et al., The molecular determinants of de novo nucleotide biosynthesis in cancer cells. Curr. Opin. Genet. Dev, 2009. 19: 32. [PubMed: 19201187]

86. Vander Heiden MG, et al., Understanding the Warburg Effect: The Metabolic Requirements of Cell Proliferation. Science 2009. 324: 1029. [PubMed: 19460998]

87. Keshari KR, et al., Hyperpolarized 13C dehydroascorbate as an endogenous redox sensor for in vivo metabolic imaging. Proc. Natl. Acad. Sci. U. S. A, 2011. 108: 18606. [PubMed: 22042839]

88. Vera JC, et al., Mammalian facilitative hexose transporters mediate the transport of dehydroascorbic acid. Nature 1993. 364: 79. [PubMed: 8316303]

89. Huang J, et al., Dehydroascorbic acid, a blood-brain barrier transportable form of vitamin C, mediates potent cerebroprotection in experimental stroke. Proc. Natl. Acad. Sci. U. S. A, 2001. 98: 11720. [PubMed: 11573006]

90. Burdon RH, Superoxide and hydrogen peroxide in relation to mammalian cell proliferation. Free Radical Biol. Med, 1995. 18: 775. [PubMed: 7750801]

91. Halliwell B, Oxidative stress in cell culture: an under-appreciated problem? FEBS Lett, 2003. 540: 3. [PubMed: 12681474]

92. Salamanca-Cardona L, et al., (13)C-labeled biochemical probes for the study of cancer metabolism with dynamic nuclear polarization-enhanced magnetic resonance imaging. Cancer Metab, 2015. 3: 9. [PubMed: 26380082]

93. Carroll VN, et al., [11C]Ascorbic and [11C]dehydroascorbic acid, an endogenous redox pair for sensing reactive oxygen species using positron emission tomography. Chem. Commun, 2016. 52: 4888.

94. Keshari KR, et al., Hyperpolarized [1–13C]dehydroascorbate MR spectroscopy in a murine model of prostate cancer: comparison with 18F-FDG PET. J. Nucl. Med, 2013. 54: 922. [PubMed: 23575993]

95. Di Marzo N, et al., The role of hydrogen peroxide in redox-dependent signaling: homeostatic and pathological responses in mammalian cells. Cells, 2018. 7: 156.

96. Sies H, Hydrogen peroxide as a central redox signaling molecule in physiological oxidative stress: Oxidative eustress. Redox Biol, 2017. 11: 613. [PubMed: 28110218]

97. Lippert AR, et al., A Hydrogen Peroxide-Responsive Hyperpolarized 13C MRI Contrast Agent. J. Am. Chem. Soc, 2011. 133: 3776. [PubMed: 21366297]

98. Wibowo A, et al., Real-Time in Vivo Detection of H2O2 Using Hyperpolarized 13C-Thiourea. ACS Chem. Biol, 2017. 12: 1737. [PubMed: 28452454]

99. Schwartz MK, Role of trace elements in cancer. Cancer Res, 1975. 35: 3481. [PubMed: 1104155]

100. Navarro SSA, et al., Trace elements and cancer risk: a review of the epidemiologic evidence. Cancer Causes Control, 2007. 18: 7. [PubMed: 17186419]

101. Serra M, et al., Understanding Metal Dynamics Between Cancer Cells and Macrophages: Competition or Synergism? Front Oncol, 2020. 10: 646. [PubMed: 32426284]

102. Ahmadi N, et al., Alterations in serum levels of trace element in patients with breast cancer before and after chemotherapy. Caspian J Intern Med, 2018. 9: 134. [PubMed: 29732030]

103. Mishra A, et al., Hyperpolarized Multi-Metal 13C-Sensors for Magnetic Resonance Imaging. Anal. Chem, 2016. 88: 10790. [PubMed: 27766840]

104. Wang S, et al., Amino Acid-Derived Sensors for Specific Zn2+ Detection Using Hyperpolarized 13C Magnetic Resonance Spectroscopy. Chem. - Eur. J, 2019. 25: 11842. [PubMed: 31338914]

105. Costello LC, et al., A comprehensive review of the role of zinc in normal prostate function and metabolism; and its implications in prostate cancer. Arch. Biochem. Biophys, 2016. 611: 100. [PubMed: 27132038]
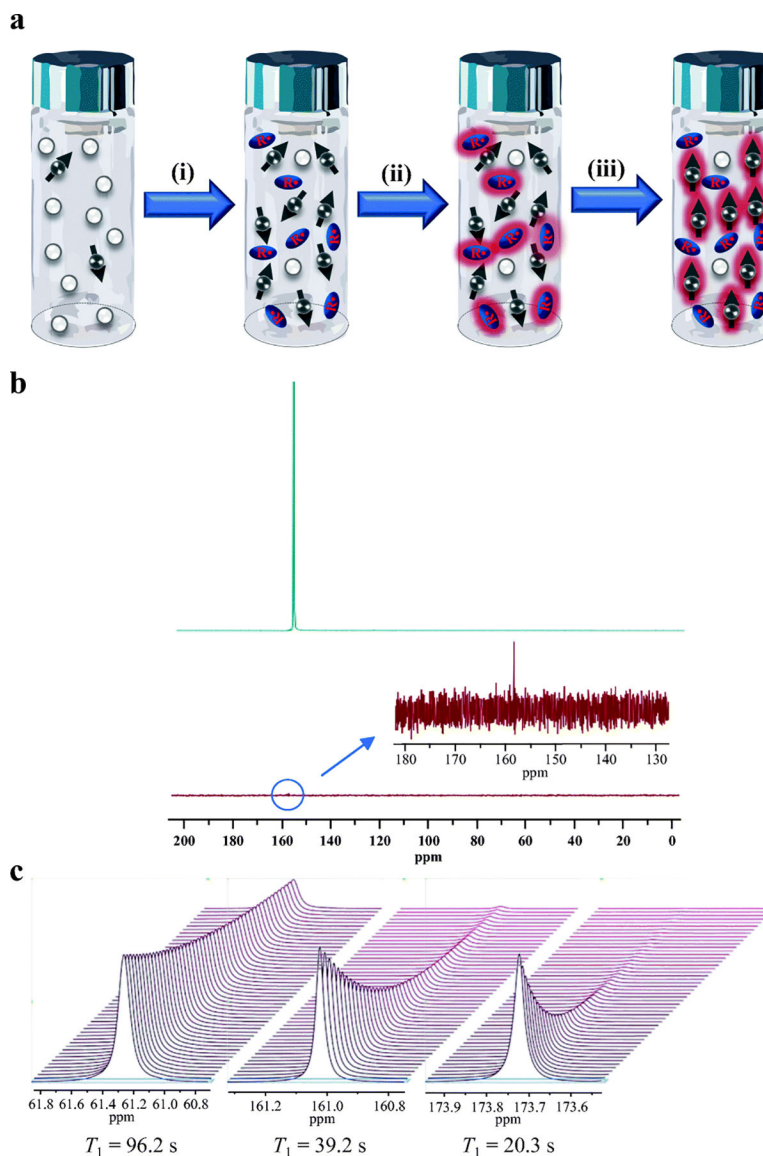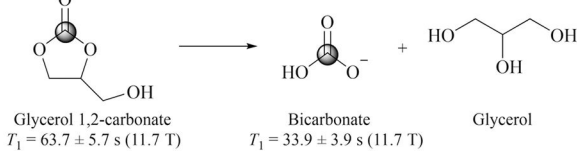
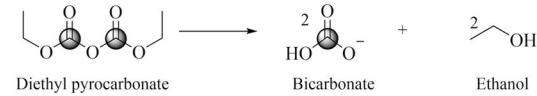**Figure 1.**
Basics of dynamic nuclear polarization. (a) Mechanism of increasing the signal to noise ratio of ^{13}C MNR via DNP: (i) preparing ^{13}C enriched biosensor molecules with stable radical species, (ii) cooling the mixture of biosensor molecules with radicals to ~1 K in a magnetic field of 3–5 T in order to generate high radical polarization, (iii) transferring the electron spin from radicals to nuclear spin on ^{13}C of biosensor molecules using microwave irradiation. (b) ^{13}C NMR spectra of ^{13}C GLC acquired at (up) HP state (29.5% polarization) with pulse angle of 15° and repetition time of 1 s based on a T_1 of 60 s with full ^1H decoupling, and (low) thermal equilibrium state. The signal is averaged of 600 transients. (c) HP ^{13}C T_1 decay spectra of (left) DEMA $T_1 = 96.2$ s, (middle) bicarbonate $T_1 = 39.2$ s, (right) DHA $T_1 = 20.3$ s. All measurements were taken at 11.7 T field strength, temporal spacing = 3s, with 500 timepoints. The large differences in SNR at later time points highlight the critical need for longer T_1 probes.

(i) ^{13}C- Biosensors for Imaging Lactate Export

Pyruvate
$T_1 = 67$ s (3 T); 48 s (11.7 T)
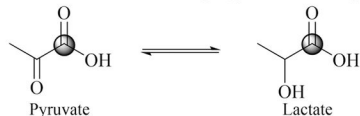
Lactate
$T_1 = 45$, 50.6 s (3 T); 32, 33.4 s (14.1 T)

(ii) ^{13}C- Biosensors for Imaging Interstitial pH

Glycerol 1,2-carbonate
$T_1 = 63.7 \pm 5.7$ s (11.7 T)

Bicarbonate
$T_1 = 33.9 \pm 3.9$ s (11.7 T)

Glycerol

Diethyl pyrocarbonate

Bicarbonate

Ethanol

2,3-O-carbonyl-a-D-mannopyranose

Bicarbonate

D-mannose

Ethyl acetyl carbonate
$T_1 = 30$ s (9.4 T)

Esterase

$^{13}CO_2$

Carbonic anhydrase

Bicarbonate

alpha-keto carboxylic acid

H_2O_2

Carboxylic acid

Bicarbonate

$^{13}CO_2$

[D$_{10}$]Diethylmalonic acid
$T_1 = 105.6 \pm 5.2$ s (11.7 T)

[D$_4$]cyclopropane -1,1-dicarboxylic acid
$T_1 = 70.2 \pm 4.5$ s (11.7 T)

Serine amide
$T_1 = 13.8 \pm 0.4$ s (1 T)

Diaminopropionic acid
$T_1 = 18.8 \pm 2.0$ s (1 T)

Alanine Ethyl Ester
$T_1 = 49$ s (3 T)

Zymonic acid
$T_1 = 43 \pm 3$ s (C$_1$), 51 $\pm$ 4 s (C$_5$) (3 T)
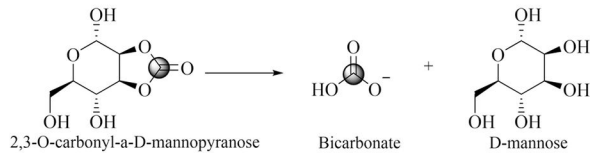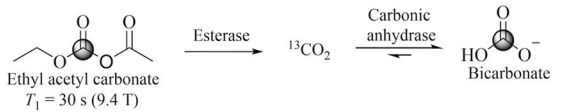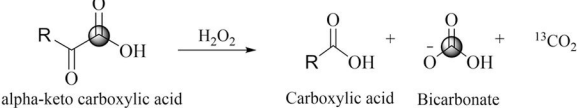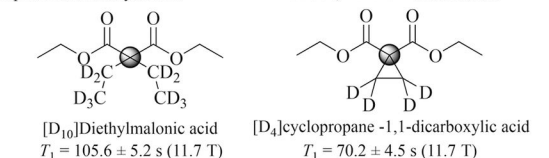
N-(2-acetamido)-2-aminoethanesulfonic acid
$T_1 = 25$ s (3 T) ,18 s (11.7 T)
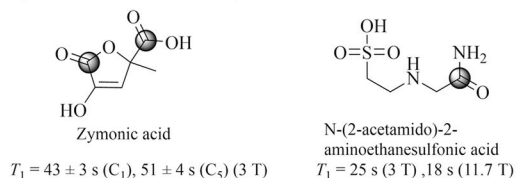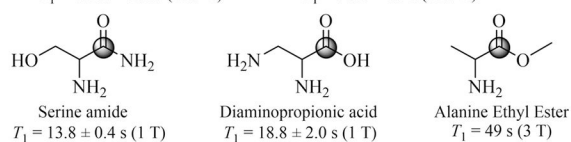
(iii) ^{13}C- Biosensors for Imaging Oxidative Stress

Ascorbic acid
$T_1 = 29$ s (3 T); 16 s (9.4, 11.7 T)

-2e-, -2H$^+$
+2e-, +2H$^+$

Dehydroascorbic acid
$T_1 = 56$ s (3 T); 21 s (9.4 T)

Acetoacetate
$T_1 = 58$ s (C$_1$), 52 s (C$_3$) (3 T)

+e-, +H$^+$
-e-, -H$^+$

ß-Hydroxybutyrate
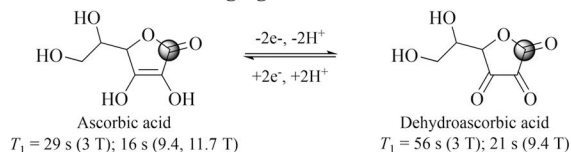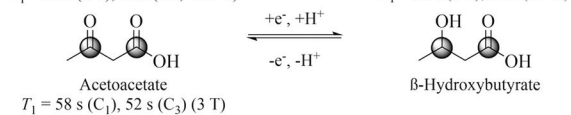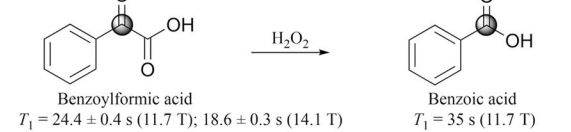
Benzoylformic acid
$T_1 = 24.4 \pm 0.4$ s (11.7 T); 18.6 $\pm$ 0.3 s (14.1 T)

H_2O_2

Benzoic acid
$T_1 = 35$ (11.7 T)

Thiourea
$T_1 = 53.8 \pm 3.7$ s (3 T)

H_2O_2

Thiourea Dioxide
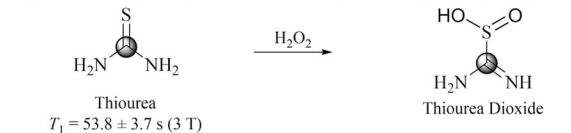
(iv) ^{13}C- Biosensors for Imaging Trace Divalent Metal Ions

EDTA
$T_1 = 13.1$ s (5.9 T)

M^{2+}

EGTA
$T_1 = 15.0$ s (5.9 T)

M^{2+}

L -cysteine
$T_1 = 36.0 \pm 1.8$ s (3T)

Zn^{2+}

Iminodiacetic acid
$T_1 = 39.3 \pm 1.0$ s (3T)

Zn^{2+}
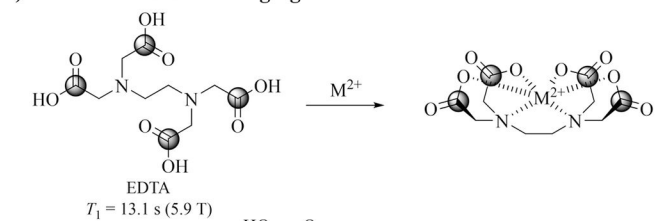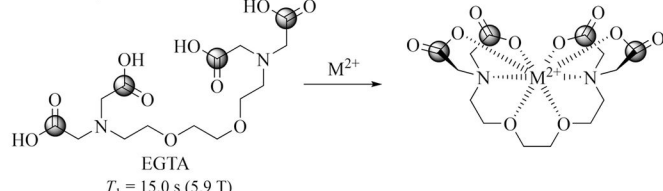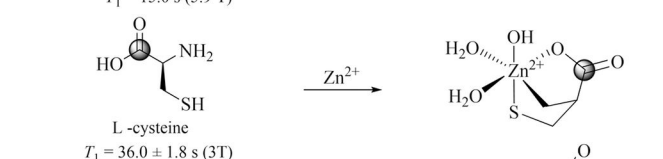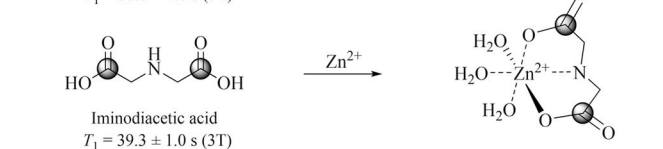
Figure 2.
^{13}C-biosensors and their proposed related reaction mechanism for imaging TME. The position of the ^{13}C label is indicated for each molecule with a circle. Published T_1 measurements are indicated.
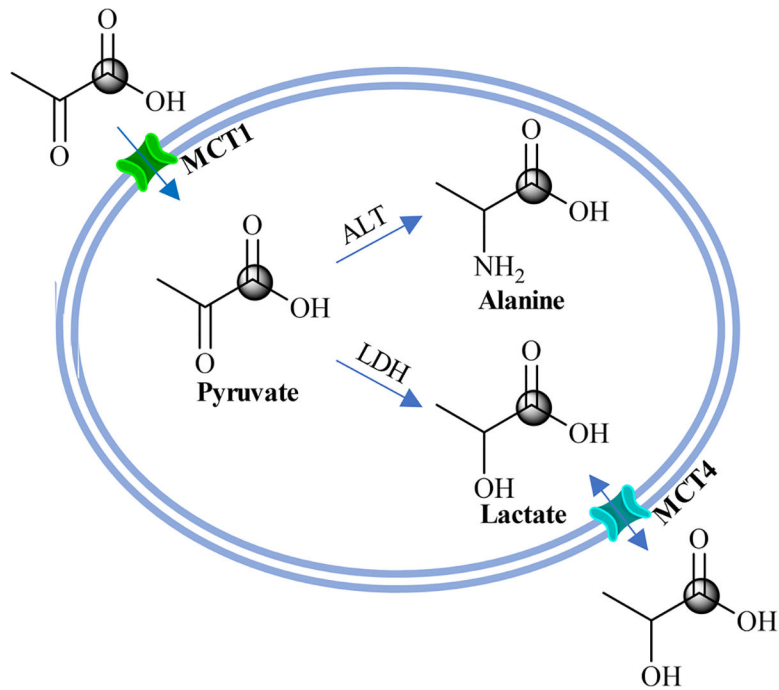
Figure 3.
Biochemical scheme illustrating the metabolic pathway of converting HP [1-^{13}C] pyruvate to HP [1-^{13}C] lactate and HP [1-^{13}C] alanine, and increased HP [1-^{13}C] lactate export into the TME via the upregulated MCT4.
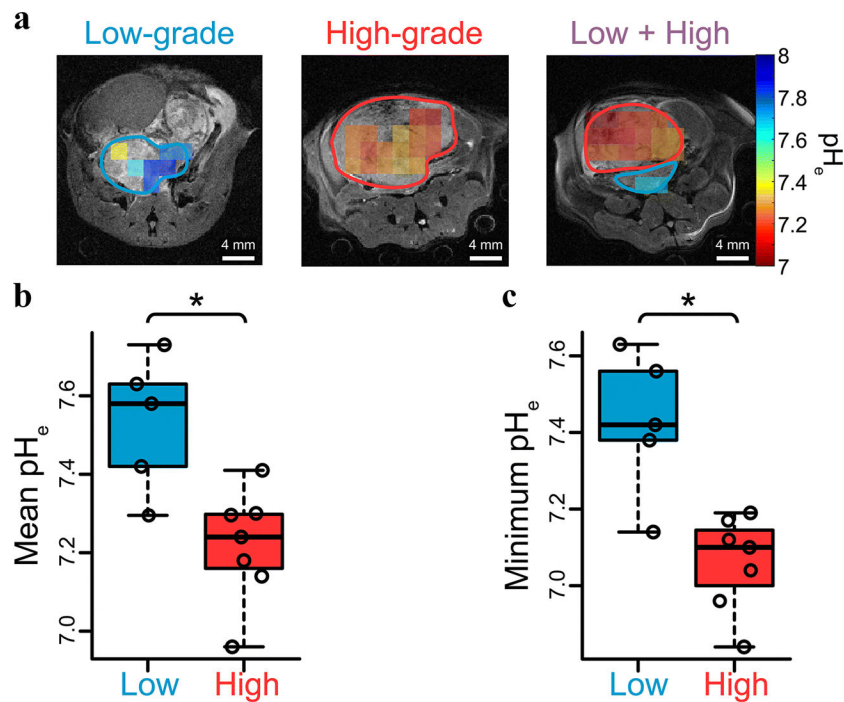
Figure 4.

DNP-MRS imaging the interstitial pHe of TRAMP mice using HP $H^{13}CO_3^-$ demonstrates decreases in tumor pH associated with high grade disease. (A) HP ^{13}C pH$_e$ images of low-, high-, and separate distinct low- and high-grade tumors in the same TRAMP mouse. High grade tumor regions verified at pathology are circled in red, and low grade regions circled in blue. (B) and (C) scatter plots demonstrating the significant difference of pH$_e$ between low- and high-grade regions over all mice on mean and regional-minimum (*p < 0.05).
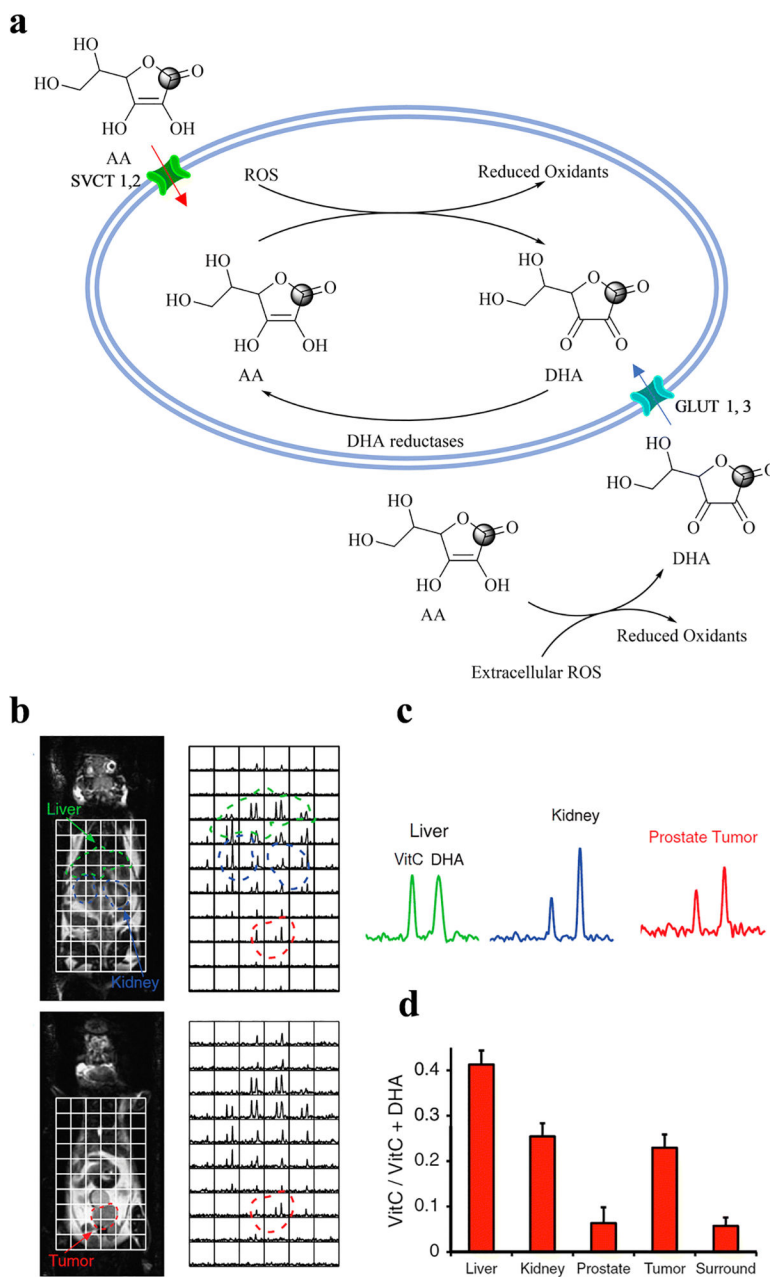
Figure 5.
The redox couple DHA and AA (VitC) is used as a biosensor for measuring oxidative stress. (a) Biochemical scheme illustrating the metabolic pathway between HP [1-^{13}C] DHA and HP [1-^{13}C] AA. HP [1-^{13}C] DHA was used as an endogenous redox sensor for *in vivo* metabolic imaging: (b) distribution of HP [1-^{13}C] AA and HP [1-^{13}C] DHA in a TRAMP mouse, (c) representative ^{13}C spectra from liver, kidney, and prostate tumor in a TRAMP mouse, and (d) summary of average metabolite ratios of HP [1-^{13}C] AA / (HP [1-^{13}C] AA)+ HP [1-^{13}C] DHA) for normal liver, kidneys, and prostate (n = 5).
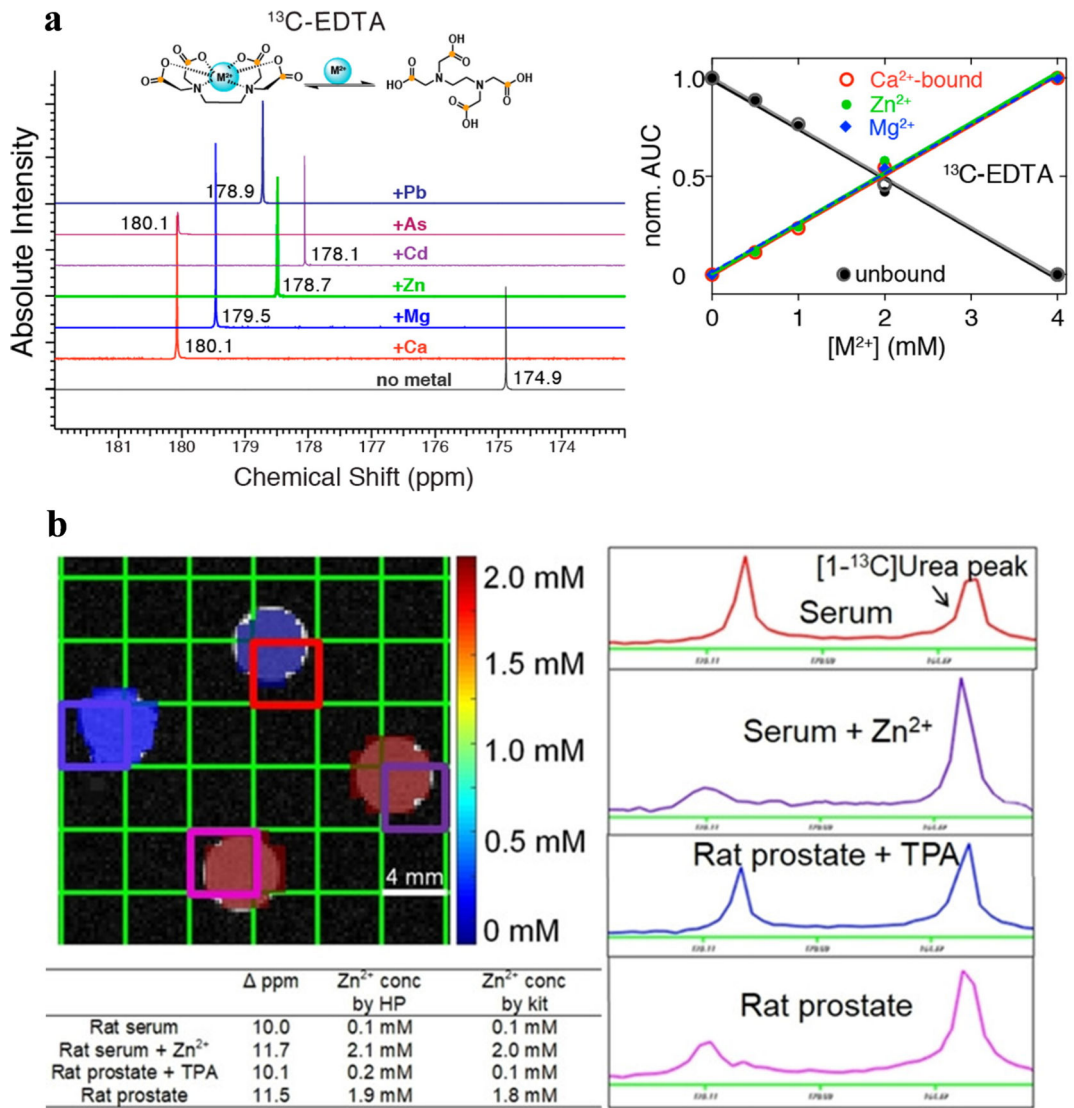
Figure 6.
(a) (left) Identification of divalent metals by metal-specific chemical shift of ^{13}C-EDTA, (right) the binding curves for different metals as plots of the area under the curve (AUC), normalized to the sum of all AUCs to the chemical shift peak originating from metal-bound or unbound ^{13}C-EDTA. (b) HP [1-^{13}C] Cys phantom imaging experiment demonstrating accurate Zn^{2+} quantification in biological samples, including serum and prostate extracts.